

Lamb Waves and Resonant Modes in Rectangular Bar Silicon Resonators

G. Casinovi, X. Gao and F. Ayazi

IEEE/ASME Journal of Microelectromechanical Systems
vol. 19, no. 4, pp. 827–839, August 2010

Abstract

This paper presents two newly developed models of capacitive silicon bulk acoustic resonators (SiBARs) characterized by a rectangular bar geometry. The first model is derived from an approximate analytical solution of the linear elastodynamics equations for a parallelepiped made of an orthotropic material. This solution, which is recognized to represent a Lamb wave propagating across the width of the resonator, yields the frequencies and shapes of the resonance modes that typically govern the operation of SiBARs. The second model is numerical and is based on finite-element, multi-physics simulation of both acoustic wave propagation in the resonator and electromechanical transduction in the capacitive gaps of the device. It is especially useful in the computation of SiBAR performance parameters that cannot be obtained from the analytical model, e.g. the relationship between transduction area and insertion loss. Comparisons with measurements taken on a set of silicon resonators fabricated using electron-beam lithography show that both models can predict the resonance frequencies of SiBARs with a relative error that in most cases is significantly smaller than 1%.

Copyright Notice

This material is presented to ensure timely dissemination of scholarly and technical work. Copyright and all rights therein are retained by authors or by other copyright holders. All persons copying this information are expected to adhere to the terms and constraints invoked by each author's copyright. In most cases, these works may not be reposted without the explicit permission of the copyright holder.

Lamb Waves and Resonant Modes in Rectangular-Bar Silicon Resonators

Giorgio Casinovi, *Senior Member, IEEE*, Xin Gao, and Farrokh Ayazi, *Senior Member, IEEE*

Abstract—This paper presents two newly developed models of capacitive silicon bulk acoustic resonators (SiBARs) characterized by a rectangular-bar geometry. The first model is derived from an approximate analytical solution of the linear elastodynamic equations for a parallelepiped made of an orthotropic material. This solution, which is recognized to represent a Lamb wave propagating across the width of the resonator, yields the frequencies and shapes of the resonance modes that typically govern the operation of SiBARs. The second model is numerical and is based on a finite-element multiphysics simulation of both acoustic wave propagation in the resonator and electromechanical transduction in the capacitive gaps of the device. It is especially useful in the computation of the SiBAR performance parameters, which cannot be obtained from the analytical model, e.g., the relationship between the transduction area and the insertion loss. Comparisons with the measurements taken on a set of silicon resonators fabricated using electron-beam lithography show that both models can predict the resonance frequencies of SiBARs with a relative error, which, in most cases, is significantly smaller than 1%. [2009-0249]

Index Terms—Computer-aided analysis, microresonators, modeling, simulation.

I. INTRODUCTION

MUCH RESEARCH activity in recent years has been directed at the development of bulk acoustic resonators (BARs) that are fully compatible with standard integrated circuit technologies. In this respect, capacitively transduced air-gap resonators [1]–[10] offer a particularly attractive option since they can be made entirely of materials that are used routinely in IC fabrication processes, resulting in significant advantages in terms of ease of integration and cost savings. Another useful feature of these resonators is that their polarization voltage can be used for several purposes such as making fine changes in their resonance frequency or turning them into narrow-band mixers or turning them on and off [9]. They can be fabricated in a single high-quality material such as a single-crystal silicon, thus eliminating the interfacial losses that beset composite structures. Furthermore, recent experimental results have shown that anchor losses can also be mitigated substantially by a careful design of the resonator geometry [11]. This makes it possible to attain very high quality factors, potentially limited only by the intrinsic losses of the material [12].

Manuscript received October 14, 2009; revised April 7, 2010; accepted April 24, 2010. Date of publication June 21, 2010; date of current version July 30, 2010. This work was supported in part by DARPA under the Analog Spectral Processors program. Subject Editor C. Nguyen.

The authors are with the School of Electrical and Computer Engineering, Georgia Institute of Technology, Atlanta, GA 30332 USA (e-mail: giorgio.casinovi@ece.gatech.edu).

Color versions of one or more of the figures in this paper are available online at <http://ieeexplore.ieee.org>.

Digital Object Identifier 10.1109/JMEMS.2010.2050862

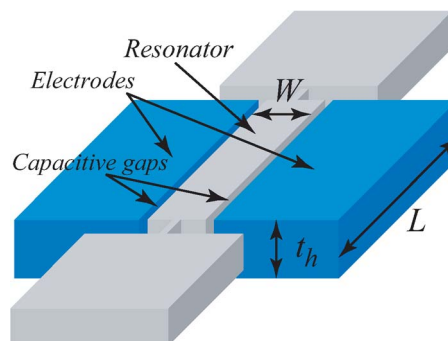


Fig. 1. Structure of a SiBAR device.

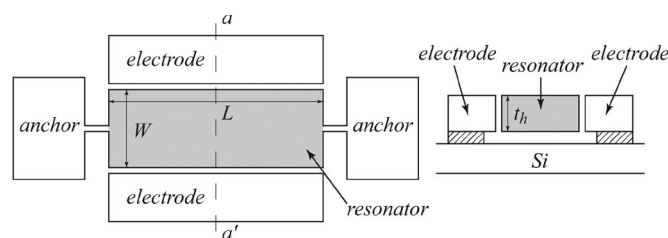


Fig. 2. (Left) Top and (right) cross-sectional views of a SiBAR.

Disk resonators were among the first examples of devices of this type [1]–[7], but more recently, air-gap capacitive resonators that are based on an alternative rectangular-bar geometry were demonstrated [8]–[10]. In this paper, they will simply be referred to as silicon BARs (SiBARs). The basic structure of such devices is shown in Figs. 1 and 2. The resonator proper is placed between two electrodes, supported by two thin tethers. The dc polarization voltage that is applied between the resonator and the electrodes generates an electrostatic field in the capacitive gaps. When an ac voltage is applied to the drive electrode, the pressure that is applied to the face of the resonator changes accordingly and induces an elastic wave that propagates through the bar. Small changes in the size of the capacitive gap on the other side of the device induce a current on the sense electrode, whose amplitude peaks near the mechanical resonance frequencies of the bar.

SiBARs offer several potential advantages over their disk-shaped counterparts. The most important of which is that the electrostatic transduction area can be increased without changing the main frequency-setting dimension, resulting in a significantly lower motional resistance while maintaining high Q values [8], [9].

Nevertheless, the equivalent impedance of SiBARs in the VHF and UHF frequency ranges remains one order of magnitude higher than that attained by piezoelectric resonators. At

the same time, it is not obvious how further reductions in the impedance of SiBARs can be achieved because it has been shown that, in some cases, an increase of the transduction area can actually result in a larger insertion loss: For instance, this happens if the SiBAR thickness exceeds certain limits [13]. To the authors' best knowledge, there is currently no quantitative analysis of the relationship between the transduction area and the insertion loss in SiBARs.

In fact, little is currently known even about the effect of the dimensions of a SiBAR on its resonance frequencies. An often-used formula is

$$f = \frac{n_z}{2W} \sqrt{\frac{E}{\rho}} \quad (1)$$

where f is the resonance frequency, n_z is the order of the resonance mode, W is the width of the resonator, and E and ρ are Young's modulus and the mass density of the material, respectively. As will be shown in this paper, however, the value of the resonance frequency that is predicted by (1) can be severely inaccurate, especially when the material is anisotropic, and therefore, it is of little use whenever accuracy is important, e.g., in the design of precision frequency references.

More accurate SiBAR models were first introduced in [14]. This paper presents an extended and more detailed analysis of those models and shows how they can be used as design aids to make further improvements in the performance of SiBARs. In particular, Section II analyzes the elastic wave propagation in a bar of rectangular cross section, which is the characteristic geometry of SiBARs. The analysis yields a set of dispersion curves representing the relationship between the propagation velocity of elastic waves and the dimensions of the resonator. Section III describes an alternative approach to the same problem, based on the Rayleigh–Ritz approximation, which is shown to yield a very similar result. The relationship obtained in Section II is used in Section IV to compute the resonance frequency sensitivities to changes in the dimensions of the resonator. Section V describes the numerical model and presents the results of the numerical simulations performed in ANSYS, which will be compared with the analytical model derived in Section II. It is also shown how the numerical model can be used to determine the value of the thickness of the resonator that minimizes the insertion loss of the device. Finally, in Section VI, both models are validated by comparing their predictions against the measurements taken on a set of devices fabricated using e-beam lithography.

II. ANALYTICAL MODEL

For analysis purposes, a SiBAR can be modeled as a parallelepiped made of a single homogeneous material. In principle, its resonance frequencies can be obtained by finding the solutions of the linear elastodynamic equations that satisfy traction-free boundary conditions on all of the faces of the parallelepiped. Unfortunately, such solutions cannot be expressed in closed form using elementary functions, not even if the material is isotropic [15, p. 223], [16, p. 460]. Consequently, any analytical model of a SiBAR must necessarily be approxi-

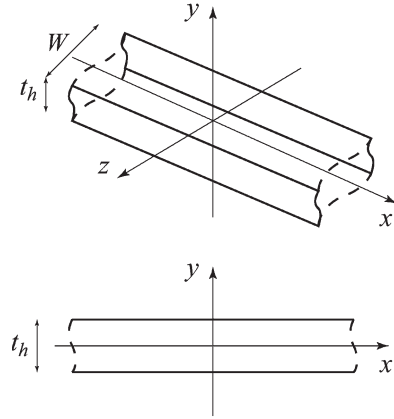


Fig. 3. Reference geometric model of a SiBAR.

mate. This section describes the derivation of one such model, which yields very accurate estimates of the frequencies of the resonance modes that are of interest in practical applications of SiBARs.

With respect to the orthogonal reference system shown in Fig. 3, the resonator dimension in the x direction will be referred to as its length (L), the one in the y direction will be referred to as its thickness (t_h), and the one in the z direction will be referred to as its width (W). For the purposes of the analysis carried out in this section and in the next, the length will be assumed to be theoretically infinite. The numerical simulation results and the experimental measurements, which will be presented in Sections V and VI, respectively, show that this assumption leads to reasonably good approximations of the actual resonance frequencies of a capacitive SiBAR, provided that the length of the resonator is sufficiently large compared to the two other dimensions. Furthermore, it will be assumed that the resonator is made of an orthotropic material whose stiffness matrix \mathbf{C} in the given reference system has the following structure:

$$\mathbf{C} = \begin{bmatrix} c_{11} & c_{12} & c_{13} & & & \\ c_{12} & c_{22} & c_{23} & & & \\ c_{13} & c_{23} & c_{33} & & & \\ & & & c_{44} & & \\ & & & & c_{55} & \\ & & & & & c_{66} \end{bmatrix}.$$

The application of a periodically varying pressure to the faces of the resonator located at $z = \pm W/2$ creates an elastic wave, whose propagation is described by the following:

$$\nabla \cdot \mathbf{T} = \rho \frac{\partial^2 \mathbf{u}}{\partial t^2} \quad (2)$$

where $\mathbf{u} = [u_x, u_y, u_z]^T$ is the displacement at a generic point in the resonator, ρ is the mass density of the material, \mathbf{T} is the stress tensor

$$\mathbf{T} = \begin{bmatrix} \sigma_{xx} & \sigma_{xy} & \sigma_{xz} \\ \sigma_{xy} & \sigma_{yy} & \sigma_{yz} \\ \sigma_{xz} & \sigma_{yz} & \sigma_{zz} \end{bmatrix}$$

and $\nabla \cdot \mathbf{T}$ represents the divergence of \mathbf{T} [17].

Since the resonator is assumed to be infinitely long, it is natural to look for solutions that are independent of x and that

have no displacement component in the x direction (i.e., $u_x = 0$). These conditions, combined with the additional requirement that \mathbf{u} should represent a sinusoidal plane wave, reduce the possible solutions of (2) to those that can be expressed in the following way:

$$\mathbf{u}(y, z, t) = \begin{bmatrix} 0 \\ u_{y0} \\ u_{z0} \end{bmatrix} e^{j(\omega t - k_y y - k_z z)}.$$

It is fairly straightforward to verify that the aforementioned expression solves (2) if and only if the following equation—generally referred to as the Christoffel equation [17]—is satisfied:

$$\begin{bmatrix} c_{22}k_y^2 + c_{44}k_z^2 - \rho\omega^2 & (c_{23} + c_{44})k_y k_z \\ (c_{23} + c_{44})k_y k_z & c_{44}k_y^2 + c_{33}k_z^2 - \rho\omega^2 \end{bmatrix} \begin{bmatrix} u_{y0} \\ u_{z0} \end{bmatrix} = 0. \quad (3)$$

Equation (3) has nontrivial solutions if and only if

$$(c_{22}k_y^2 + c_{44}k_z^2 - \rho\omega^2)(c_{44}k_y^2 + c_{33}k_z^2 - \rho\omega^2) - [k_y k_z (c_{23} + c_{44})]^2 = 0.$$

By expanding the product terms and dividing through by k_z^4 , the aforementioned equation can be rewritten in equivalent form as

$$\begin{aligned} c_{22}c_{44}\zeta^2 + [c_{44}^2 + c_{22}c_{33} - (c_{23} + c_{44})^2 \\ - \rho(c_{22} + c_{44})v^2] \zeta + \rho^2 v^4 \\ - (c_{33} + c_{44})\rho v^2 + c_{33}c_{44} = 0 \end{aligned} \quad (4)$$

where $\zeta = (k_y/k_z)^2$ and $v = \omega/k_z$. For a given value of v , there are, in general, two solutions to (4), regarded as an equation in ζ ; hence, there are four values of the ratio k_y/k_z for which (3) has nontrivial solutions. For the wave to propagate in the z direction, k_z must be a real number, but k_y may be real or complex, depending on whether the solutions of (4) are complex or real and, in the latter case, whether they are positive or negative. Physically, a purely imaginary value of k_y corresponds to a wave of constant amplitude in the y direction (i.e., across the thickness of the resonator), while a real negative (positive) value of k_y corresponds to a wave whose amplitude decreases exponentially in the positive (negative) y direction.

It is readily observed that the constant term in (4) (i.e., the term that is independent of ζ) can also be written as $(\rho v^2 - c_{33})(\rho v^2 - c_{44})$. Let $v_u = \sqrt{c_{33}/\rho}$ and $v_l = \sqrt{c_{44}/\rho}$. Note that $v_l \leq v_u$ because $c_{44} \leq c_{33}$. Consequently, if $v_l \leq v \leq v_u$, the constant term in (4) is negative, which means that, in this case, (4) has two real solutions (one positive and one negative). By letting $\zeta_1 = -\alpha^2$ and $\zeta_2 = \beta^2$, the possible values for k_y are $\pm j\alpha k_z$ and $\pm\beta k_z$, and for each of them, the corresponding values of u_{y0} and u_{z0} can be obtained from (3). For example, if $k_y = j\alpha k_z$, then one can set

$$u_{y0} = j\alpha \quad u_{z0} = \frac{\rho v^2 + c_{22}\alpha^2 - c_{44}}{c_{23} + c_{44}}$$

and the corresponding sinusoidal steady-state solution of (2) is given by

$$\mathbf{u}(y, z, t) = \begin{bmatrix} j\alpha \\ u_{z0} \end{bmatrix} e^{\alpha k_z y} e^{j(\omega t - k_z z)}$$

where the x component of \mathbf{u} , which is equal to zero, has been omitted to simplify the notation. Similarly, if $k_y = \beta k_z$, the sinusoidal steady-state solution is given by

$$\mathbf{u}(y, z, t) = \begin{bmatrix} -u_{y1} \\ \beta \end{bmatrix} e^{-j\beta k_z y} e^{j(\omega t - k_z z)}$$

where

$$u_{y1} = \frac{c_{44}\beta^2 + c_{33} - \rho v^2}{c_{23} + c_{44}}.$$

Solutions that correspond to the other values of k_y can simply be obtained by changing the signs of α and β in the aforementioned expressions.

The general solution of (2) is given by the linear combination of the solutions that correspond to the four possible values of k_y . The space of possible solutions can be reduced further by observing that, in most practical applications, the pressure on the faces of the resonator that correspond to the planes $z = \pm W/2$ is applied in a way that is symmetric with respect to the plane $y = 0$. This means that the z component of the displacement must also be symmetric with respect to the same plane (i.e., u_z must satisfy the relationship $u_z(-y, z, t) = u_z(y, z, t)$). Imposing this requirement on \mathbf{u} leads to the following solution for (2):

$$\begin{aligned} \mathbf{u}(y, z, t) = A_0 \begin{bmatrix} j\alpha \sinh(\alpha k_z y) \\ u_{z0} \cosh(\alpha k_z y) \end{bmatrix} e^{j(\omega t - k_z z)} \\ + A_1 \begin{bmatrix} j u_{y1} \sin(\beta k_z y) \\ \beta \cos(\beta k_z y) \end{bmatrix} e^{j(\omega t - k_z z)}. \end{aligned} \quad (5)$$

This solution represents a symmetric Rayleigh–Lamb wave propagating in the z direction (i.e., across the width of the resonator).

Coefficients A_0 and A_1 in (5) must be chosen so that \mathbf{u} satisfies the traction-free boundary conditions on the top and bottom faces of the resonator, i.e.,

$$\sigma_{xy} = \sigma_{yy} = \sigma_{yz} = 0, \quad y = \pm t_h/2 \quad (6)$$

where

$$\begin{aligned} \sigma_{xy} &= c_{66} \left(\frac{\partial u_x}{\partial y} + \frac{\partial u_y}{\partial x} \right) \\ \sigma_{yy} &= c_{12} \frac{\partial u_x}{\partial x} + c_{22} \frac{\partial u_y}{\partial y} + c_{23} \frac{\partial u_z}{\partial z} \\ \sigma_{yz} &= c_{44} \left(\frac{\partial u_y}{\partial z} + \frac{\partial u_z}{\partial y} \right). \end{aligned}$$

It is immediate to verify that $\sigma_{xy} = 0$, regardless of the values of A_0 and A_1 . After some algebraic manipulation, the two remaining conditions translate into the following system of equations in unknowns A_0 and A_1 :

$$\begin{aligned} (c_{22}\alpha^2 - c_{23}u_{z0}) \cosh(\alpha k_z t_h/2) A_0 \\ + \beta(c_{22}u_{y1} - c_{23}) \cos(\beta k_z t_h/2) A_1 = 0 \\ \alpha(1 + u_{z0}) \sinh(\alpha k_z t_h/2) A_0 \\ + (u_{y1} - \beta^2) \sin(\beta k_z t_h/2) A_1 = 0. \end{aligned}$$

This system has nontrivial solutions only if the determinant of the coefficient matrix is equal to zero. By making the

substitution $k_z = 2\pi/\lambda_z$, where λ_z is the wavelength in the z direction, this condition yields the following equation:

$$(c_{22}\alpha^2 - c_{23}u_{z0})(u_{y1} - \beta^2) \cosh(\pi\alpha\xi) \sin(\pi\beta\xi) - \alpha\beta(1 + u_{z0})(c_{22}u_{y1} - c_{23}) \sinh(\pi\alpha\xi) \cos(\pi\beta\xi) = 0 \quad (7)$$

where $\xi = t_h/\lambda_z$. For fixed α and β , this is an equation in ξ , which has infinitely many solutions, because of the periodicity of the sine and cosine terms.

Since α and β depend on v through (4), (4) and (7), taken together, define implicitly a relationship between v and ξ . Since (7) has multiple solutions, this relationship defines a function $v = v(\xi)$ that has multiple branches. In other words, the relationship between ξ and v is represented by multiple dispersion curves, and each curve corresponds to a different mode of propagation of elastic waves across the resonator. For each point (ξ, v) that lies on one of those curves, it is possible to choose A_0 and A_1 so that the solution of (2), which is defined by (5), satisfies the boundary conditions (6). Thus, each point on one of the dispersion curves identifies an elastic wave that propagates across the resonator in the positive z direction.

As mentioned at the beginning of this section, the resonance modes of the resonator correspond to a combination of elastic waves propagating in either the positive or negative z direction, which satisfy the traction-free boundary conditions on all of the resonator surfaces. This means that, in addition to (6), such combination of waves would also have to satisfy the boundary conditions

$$\sigma_{xz} = \sigma_{yz} = \sigma_{zz} = 0, \quad z = \pm W/2.$$

It is easily verified that any wave of the type given by (5) satisfies the condition $\sigma_{xz} = 0$. On the other hand, somewhat lengthy but straightforward calculations, which are omitted here, reveal that no combination of a finite number of those waves can satisfy the remaining two conditions at the same time. If $\sin k_z W = 0$, however, it is possible to combine two waves of the type in (5), with one propagating in the positive and the other in the negative z direction, so that the resulting wave satisfies either the condition $\sigma_{yz} = 0$ or $\sigma_{zz} = 0$ (but not both). This observation suggests that (5) may yield a reasonably close approximation of a resonance mode when $k_z W = n_z \pi$ or, equivalently, $\lambda_z = 2W/n_z$. This hypothesis is confirmed by the numerical simulation and experimental results reported in Sections V and VI, respectively.

The expression for \mathbf{u} in (5) and the relationship between v and ξ derived from (7) are valid only for $v_l \leq v \leq v_u$, but the procedure outlined earlier requires only minor modifications to handle other values of v . If $v \geq v_u$, both solutions of (4) are real and positive. Then, $k_y = \pm\alpha k_z$, or $k_y = \pm\beta k_z$, and the expression for \mathbf{u} becomes

$$\mathbf{u}(y, z, t) = A_0 \begin{bmatrix} j\alpha \sin(\alpha k_z y) \\ u_{z0} \cos(\alpha k_z y) \end{bmatrix} e^{j(\omega t - k_z z)} + A_1 \begin{bmatrix} j u_{y1} \sin(\beta k_z y) \\ \beta \cos(\beta k_z y) \end{bmatrix} e^{j(\omega t - k_z z)} \quad (8)$$

where

$$u_{z0} = \frac{c_{22}\alpha^2 - \rho v^2 + c_{44}}{c_{23} + c_{44}}$$

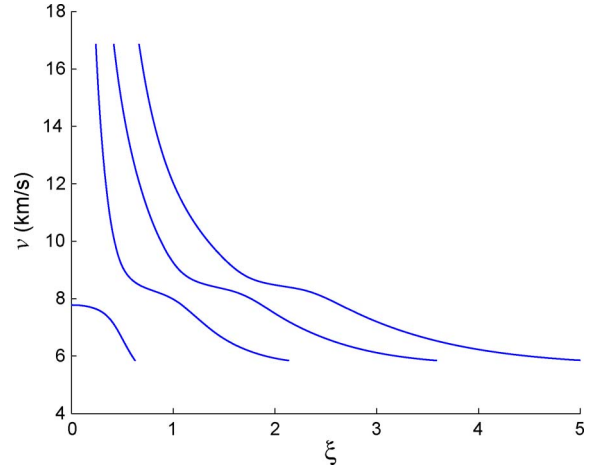


Fig. 4. Wave propagation velocity in an infinitely long (100, 010) SiBAR. The values of the elastic constants that were used to obtain this graph are $c_{22} = 165.7$, $c_{23} = 63.9$, and $c_{44} = 79.6$ GPa [18].

and u_{y1} is the same as before. In this case, the boundary conditions in (6) are satisfied by nontrivial values of A_0 and A_1 if

$$(c_{22}\alpha^2 - c_{23}u_{z0})(u_{y1} - \beta^2) \cos(\pi\alpha\xi) \sin(\pi\beta\xi) - \alpha\beta(1 - u_{z0})(c_{22}u_{y1} - c_{23}) \sin(\pi\alpha\xi) \cos(\pi\beta\xi) = 0. \quad (9)$$

This equation defines a relationship between ξ and v that is valid for $v \geq v_u$. Analogous equations for the case $v \leq v_l$ can be obtained in a similar manner.

It should be noted that the relationship between ξ and v , which is defined by (7) and (9), depends only on the properties of the material and, if the material is not isotropic, on the direction of the propagation of the wave. It follows that the propagation velocity of the elastic waves in a SiBAR depends on the orientation of the resonator with respect to the main crystallographic axes of silicon. In this paper, such orientation will be identified, as illustrated by the following example: A (100, 010) SiBAR will denote a resonator fabricated in a (100) wafer—which implies that the y axis in Fig. 3 coincides with the [100] crystallographic axis—and in which the direction of the propagation of the waves (the z axis in Fig. 3) coincides with the [010] crystallographic axis.

Figs. 4 and 5 show the dispersion curves representing the relationship between ξ and v in (100, 010) and (100, 011) SiBARs, respectively. Only the first four of infinitely many dispersion curves are shown in the figures. The graph shown in Fig. 6 corresponds to a hypothetical isotropic material whose Young's modulus and Poisson's ratio correspond to those of silicon in the [011] direction of the (100) plane. A comparison of this figure with the previous ones shows clearly that an isotropic model does not yield a sufficiently accurate description of elastic wave propagation in SiBARs.

As shown in the figures, only the first dispersion curve approaches a finite value v_0 as ξ tends to zero. In the case of an isotropic material, this value can be computed explicitly, and it is given by

$$v_0 = 2\sqrt{\frac{\mu(\lambda + \mu)}{\rho(\lambda + 2\mu)}} = \sqrt{\frac{E}{\rho(1 - \nu^2)}}$$

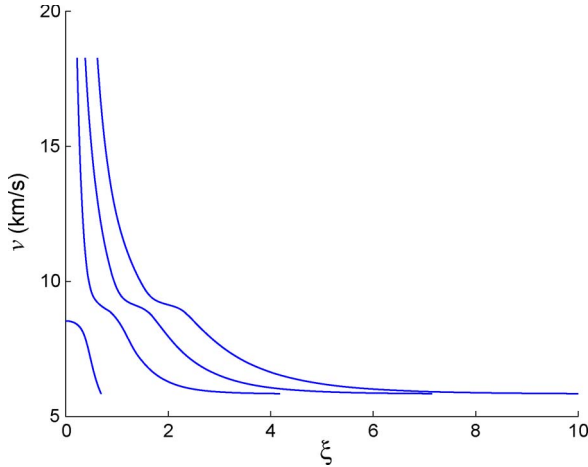


Fig. 5. Wave propagation velocity in an infinitely long (100, 011) SiBAR. The values of the elastic constants that were used to obtain this graph are $c_{22} = 165.7$, $c_{33} = 194.4$, $c_{23} = 63.9$, and $c_{44} = 79.6$ GPa.

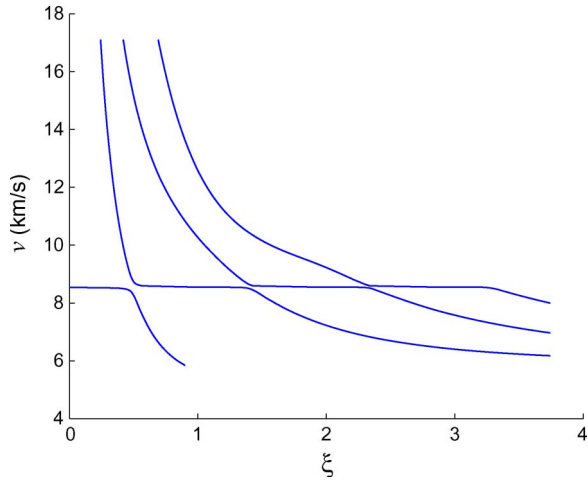


Fig. 6. Wave propagation velocity in an infinitely long rectangular-bar resonator that is made of a hypothetical isotropic material with $E = 169$ GPa and $\nu = 0.0622$.

where λ and μ are the Lamé constants, E is Young's modulus, and ν is Poisson's ratio of the material. For a general orthotropic material, the equations that define the value of v_0 become too complex to be solved analytically, and the computation must be performed numerically.

Let α_u and β_u denote the values of α and β when $v = v_u$. It is relatively straightforward to verify that $\alpha_u = 0$ and $\beta_u^2 = [(c_{23} + c_{44})^2 + c_{44}(c_{33} - c_{44})]/c_{22}c_{44}$. It follows that all of the dispersion curves, except the first one, intersect the line $v = v_u$ when $\sin \pi \beta_u \xi = 0$ (i.e., for $\xi = n_y/\beta_u$, $n_y = 1, 2, \dots$).

The behavior of $v(\xi)$ as v approaches v_l is more complex, and it depends on the sign of the nonzero solution of (4) when $v = v_l$, which is given by

$$\zeta_l = \frac{(c_{23} + c_{44})^2 - c_{22}(c_{33} - c_{44})}{c_{22}c_{44}}.$$

Let α_l and β_l denote the values of α and β when $v = v_l$. If $\zeta_l < 0$, which is always the case if the material is isotropic, then $\alpha_l^2 = -\zeta_l$, and $\beta_l = 0$. After a considerable amount of algebraic manipulation, it can then be shown that $v(\xi) = v_l$ if

$$a\eta = \tanh(\eta) \quad (10)$$

where $\eta = \alpha_l \pi \xi$ and

$$a = \frac{c_{22}c_{44}^2(c_{33} - c_{44})}{[c_{22}(c_{33} - c_{44}) - c_{23}(c_{23} + c_{44})]^2}.$$

If $a < 1$, which, once again, is always the case if the material is isotropic, (10) has exactly one positive solution, which means that only the first dispersion curve intersects the line $v = v_l$, while all the others remain above it. If $a \geq 1$, (10) has no positive solutions, and in this case, the inequality $v(\xi) > v_l$ always holds.

If $\zeta_l > 0$, then $\alpha_l = 0$, and $\beta_l^2 = \zeta_l$. In this case, the condition $v(\xi) = v_l$ translates into the following equation:

$$a\eta = \tan(\eta) \quad (11)$$

where $\eta = \beta_l \pi \xi$ and a is given by the same expression as before. Since this equation has infinitely many solutions, all of the dispersion curves intersect the line $v = v_l$.

Once $v(\xi)$ for a particular material has been computed, it is straightforward to relate it to the resonance frequencies of a resonator of given dimensions. By definition, $v = \omega/k_z$, and $k_z = 2\pi/\lambda_z$, and from these two equalities, it follows that $f\lambda_z = v$. As explained earlier in this section, approximately resonant conditions are obtained when λ_z is an integer submultiple of $2W$ (i.e., $\lambda_z = 2W/n_z$); hence,

$$f = \frac{1}{\lambda_z} v(\xi) = \frac{n_z}{2W} v[(n_z/2W)t_h]. \quad (12)$$

Therefore, the relationship between the resonator dimensions and its resonance frequencies can be obtained from $v(\xi)$ simply by changing the scales on the v and ξ axes. Of course, (12) is not necessarily valid for all possible resonance modes, but it is valid only for those that satisfy the assumptions made in the derivation of $v(\xi)$. As stated earlier in this section, those modes are associated with symmetric Rayleigh–Lamb waves that propagate across the width of the resonator and that are characterized by having a zero displacement in the direction of the resonator length ($u_x = 0$) and displacements that are independent of x in the other two directions.

It should also be pointed out that the various dispersion curves indicate only the potential existence of resonance modes. In other words, given an arbitrary point on one of the dispersion curves, there is no guarantee that a resonance mode that corresponds to that point actually exists. Even if such mode exists, it may generate only a small peak or even no peak at all in the electrical frequency response of the device, for reasons related to electromechanical transduction in the capacitive gaps that are explained in more detail in Section V. To the authors' best knowledge, all SiBARs that have been fabricated to date operate on the first dispersion curve: Whether SiBAR operation on the other curves is possible in practice is still an open question.

In theory, the analysis carried out in this section applies only to infinitely long resonators. In practice, it yields very good approximations of the actual resonance frequencies of devices even with a relatively small length-to-width ratio. This can be evinced from the numerical simulation results that are reported in Section V (and specifically in Fig. 16), which show that the analytical model can predict the resonance frequencies of

(100, 011) SiBARs having length-to-width ratios ranging from 2 to 12, with a relative error (with respect to the numerical ANSYS simulations) that is typically on the order of 0.1% or less. These results are validated by the experimental data reported in Section VI.

III. RAYLEIGH–RITZ APPROXIMATION

The Rayleigh–Ritz method is often used to obtain approximate values for the resonance frequencies of an elastic body when it is impossible or impractical to compute the exact solution to the elastodynamic equations. In its simplest form, the Rayleigh–Ritz method is based on the fact that, in sinusoidal steady state and at resonance, a constant amount of energy is being constantly transformed from potential into kinetic and back. This principle translates into the equality $T = U$, where T and U are phasors representing the kinetic and potential energies of the body, respectively [19].

In this section, the Rayleigh–Ritz method will be used to obtain approximate values for the resonance frequencies of a SiBAR, under the same assumptions as those made in the previous section. This will serve both to confirm the earlier derivation and to provide an alternate and somewhat simpler procedure than the one described in Section II. For simplicity, the analysis will be limited to the range $v_l \leq v \leq v_u$, which is the most likely region of operation for the device.

By assuming a sinusoidal steady state and by using a phasor notation, the kinetic energy of the resonator that is due to elastic vibration is given by

$$\begin{aligned} T &= \frac{1}{2} \int_V \rho (|\dot{u}_x|^2 + |\dot{u}_y|^2 + |\dot{u}_z|^2) dv \\ &= \frac{\omega^2}{2} \int_V \rho (|u_x|^2 + |u_y|^2 + |u_z|^2) dv \end{aligned}$$

where the integral is evaluated over the volume of the resonator. The elastic potential energy of the resonator can be expressed in terms of strains and stresses as follows:

$$U = \frac{1}{2} \int_V \sum_{p,q=\{x,y,z\}} \sigma_{pq} \bar{\varepsilon}_{pq} dv$$

where $\bar{\varepsilon}_{pq}$ denotes the complex conjugate of the strain tensor component $\varepsilon_{pq} = (\partial u_p / \partial q + \partial u_q / \partial p) / 2$.

The expressions for T and U given earlier must then be evaluated using a suitable approximation for the solution of (2). This is a critical step because it affects directly the accuracy of the value of the resonance frequency yielded by the Rayleigh–Ritz method. Therefore, the goal must be to choose an expression for \mathbf{u} that is sufficiently close to (5)—the exact solution of (2)—yet easier to obtain. Note that $\alpha \approx 0$ for $v \approx v_u$, and in this case, $\sinh(\alpha k_z y) \approx \alpha k_z y$, and $\cosh(\alpha k_z y) \approx 1$. Hence, a suitable expression for \mathbf{u} appears to be the following:

$$\begin{aligned} k_z \mathbf{u}(y, z, t) &= \begin{bmatrix} 0 \\ 1 \end{bmatrix} e^{j(\omega t - k_z z)} + A_0 \begin{bmatrix} j k_z y \\ u_{z0} \end{bmatrix} e^{j(\omega t - k_z z)} \\ &\quad + A_1 \begin{bmatrix} j u_{y1} \sin(\beta k_z y) \\ \beta \cos(\beta k_z y) \end{bmatrix} e^{j(\omega t - k_z z)}. \end{aligned} \quad (13)$$

To improve the accuracy of this expression, the values of u_{z0} and u_{y1} should be chosen so that each term in (13), taken individually, is a solution of (2) for some values of ω . This requirement leads to the following expressions:

$$\begin{aligned} u_{z0} &= \frac{c_{23} + c_{44}}{c_{33} - c_{44}} \\ u_{y1} &= \frac{c_{44} \beta^2 + c_{33} - \gamma}{c_{23} + c_{44}} \end{aligned}$$

where γ is the smallest eigenvalue of the following matrix:

$$\begin{bmatrix} c_{22} \beta^2 + c_{44} & -(c_{23} + c_{44}) \beta \\ -(c_{23} + c_{44}) \beta & c_{44} \beta^2 + c_{33} \end{bmatrix}.$$

Note that the expression for \mathbf{u} given in (13) is not necessarily a solution of (2) because, in general, each term in (13) solves (2) for a different value of ω .

The values of A_0 and A_1 should be chosen so that the boundary conditions in (6) are satisfied. By proceeding as in Section II, this requirement yields the following system of equations:

$$\begin{aligned} (k_z t_h / 2) A_0 + (u_{y1} - \beta^2) \sin(\beta k_z t_h / 2) A_1 &= 0 \\ (c_{22} - c_{23} u_{z0}) A_0 + (c_{22} u_{y1} - c_{23}) \beta \cos(\beta k_z t_h / 2) A_1 &= c_{23}. \end{aligned}$$

These conditions still leave one parameter undetermined, namely, the value of $\beta = k_y / k_z$. One possible way to select this value is to require $\cos(k_y t_h / 2) = \cos(\pi \beta \xi) = 0$, which yields $\beta = (n_y - 1/2) / \xi$, where $n_y = 1, 2, \dots$, depending on what dispersion curve is being approximated.

Once the values of all the parameters in the expression for \mathbf{u} have been computed, T and U can be evaluated from the expressions given earlier. In this case, several stresses are equal to zero, and the expression for the potential energy reduces to

$$\begin{aligned} U &= \frac{1}{2} \int_V (\sigma_{yy} \bar{\varepsilon}_{yy} + \sigma_{zz} \bar{\varepsilon}_{zz} + 2\sigma_{yz} \bar{\varepsilon}_{yz}) dv \\ &= \frac{1}{2} \int_V [c_{22} |\varepsilon_{yy}|^2 + c_{23} (\bar{\varepsilon}_{yy} \varepsilon_{zz} + \varepsilon_{yy} \bar{\varepsilon}_{zz}) \\ &\quad + c_{33} |\varepsilon_{zz}|^2 + 4c_{44} |\varepsilon_{yz}|^2] dv. \end{aligned}$$

Then, the equality $T = U$ yields

$$v^2 = \frac{\omega^2}{k_z^2} = \frac{2U}{k_z^2 \int_V \rho (|u_x|^2 + |u_y|^2 + |u_z|^2) dv}. \quad (14)$$

The aforementioned equation can be used to compute the dispersion curves for those resonance modes that can be reasonably approximated by (13). Because of the way in which (13) was arrived at, those are the modes that satisfy the assumptions stated in Section II.

Fig. 7 shows the first two dispersion curves for a (100, 010) SiBAR. For comparison purposes, the corresponding curves from Fig. 4 are also shown (dashed lines). The same comparison for a (100, 011) SiBAR is shown in Fig. 8. It can be seen that the two methods are in excellent agreement on the upper portion of the first curve, while some difference is noticeable on the second dispersion curve, especially at the beginning. This discrepancy can be taken as an indication that

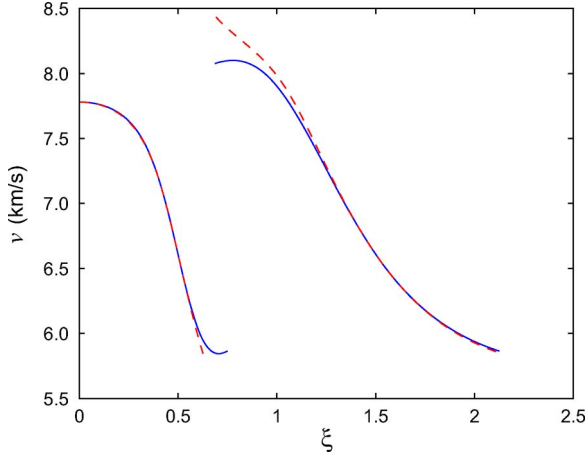


Fig. 7. Dispersion curves for a (100, 010) SiBAR obtained from (solid lines) the Rayleigh–Ritz method and (dashed lines) the method in Section II.

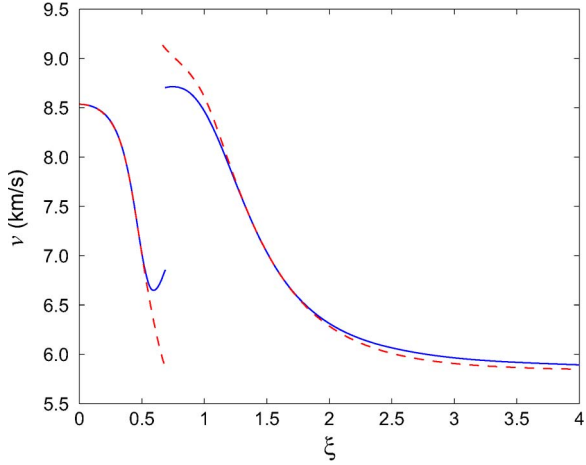


Fig. 8. Dispersion curves for a (100, 011) SiBAR obtained from (solid lines) the Rayleigh–Ritz method and (dashed lines) the method in Section II.

the equation $\beta = (n_y - 1/2)/\xi$ is not a sufficiently accurate model of the actual relationship between β and ξ , except on the first dispersion curve.

IV. FREQUENCY SENSITIVITY TO PROCESS VARIATIONS

Changes in the resonance frequency of a BAR that are caused by variations in its dimensions, which are unavoidable in integrated circuit fabrication, are an important issue in many practical applications. Using the results obtained in Section II, it is possible to obtain analytical expressions for the sensitivity of the resonance frequency to changes in the width and thickness of the resonator. Specifically, it is readily seen from (12) that, under the assumptions spelled out in Section II, the resonance frequency depends on W and t_h only through λ_z and ξ . Hence,

$$\begin{aligned} \frac{\partial f}{\partial W} &= \frac{df}{d\lambda_z} \frac{d\lambda_z}{dW} = \frac{2}{n_z} \left[-\frac{1}{\lambda_z^2} v(\xi) + \frac{1}{\lambda_z} \frac{dv}{d\xi} \frac{d\xi}{d\lambda_z} \right] \\ &= -\frac{2}{n_z \lambda_z^2} [v(\xi) + \xi v'(\xi)] \\ \frac{\partial f}{\partial t_h} &= \frac{1}{\lambda_z} \frac{dv}{d\xi} \frac{d\xi}{dt_h} = \frac{1}{\lambda_z^2} v'(\xi) \end{aligned}$$

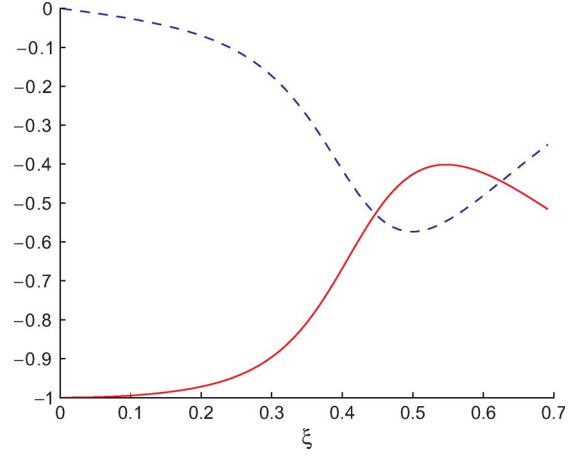


Fig. 9. Graphs of (solid line) $-[1 + v'(\xi)/v(\xi)]$ and (dashed line) $v'(\xi)/[2v(\xi)]$ for the first dispersion curve of a (100, 011) SiBAR.

where $v'(\xi)$ denotes the derivative of $v(\xi)$. Then, the relative changes in the resonance frequency due to small variations in W and t_h are given by

$$\left(\frac{\Delta f}{f} \right)_W \approx \frac{1}{f} \left(\frac{\partial f}{\partial W} \right) \Delta W = - \left(1 + \frac{v'(\xi)}{v(\xi)} \right) \frac{\Delta W}{W} \quad (15)$$

$$\left(\frac{\Delta f}{f} \right)_{t_h} \approx \frac{1}{f} \left(\frac{\partial f}{\partial t_h} \right) \Delta t_h = n_z \left(\frac{v'(\xi)}{2v(\xi)} \right) \frac{\Delta t_h}{W}. \quad (16)$$

These equations show that the relative changes in the value of f are proportional to $(\Delta W/W)$ and $(\Delta t_h/W)$ through factors that are determined by the ratio $v'(\xi)/v(\xi)$. Of course, this ratio depends on what dispersion curve the resonator is operating on. Additionally, the sensitivity of f to changes in the thickness is proportional to n_z , which is the order of the mode with respect to the direction of propagation. In the particular case of thin resonators operating on the first dispersion curve, for which $\xi \approx 0$, the aforementioned equations reduce to $(\Delta f/f)_W \approx -(\Delta W/W)$ and $(\Delta f/f)_{t_h} \approx 0$, respectively, because $v'(0) = 0$.

For reference purposes, Fig. 9 shows the graphs of $-[1 + v'(\xi)/v(\xi)]$ and $v'(\xi)/[2v(\xi)]$ for the first dispersion curve of a (100, 011) SiBAR. As shown in that figure, the magnitude of both functions is on the order of unity. The corresponding graphs for a (100, 010) SiBAR look similar, and they are not shown here for space reasons. Therefore, as a rough approximation, it can be assumed that the relative changes in the resonance frequency of a SiBAR that are due to changes in its width and thickness are approximately on the same order of magnitude as $(\Delta W/W)$ and $(\Delta t_h/W)$, respectively.

V. FINITE-ELEMENT MODEL

The analytical models described in the preceding sections rest on a number of simplifying assumptions, most notably on the resonator being of infinite length. Moreover, those models describe only the mechanical dynamics of the resonator, leaving out the electrostatic transduction effect in the capacitive gaps, which is an integral aspect of the behavior of the device. The development of an analytical model that includes the transduction effect and that also accounts for the finite length of the

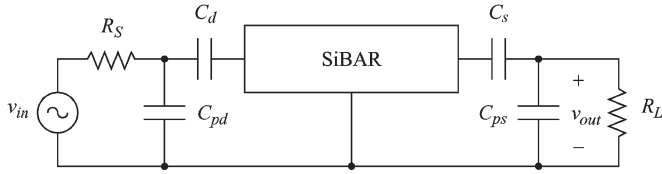


Fig. 10. Equivalent circuit of the ANSYS model, including the test setup.

resonator is a very challenging task because of the mathematical complexities involved. On the other hand, it is relatively easier to model those effects numerically using multiphysics simulation software. This section describes one such model, developed using the ANSYS simulator, and presents the simulation results obtained from it. On the basis of these results, it is possible to make a preliminary assessment of the accuracy of the analytical model described in Section II and, in particular, of the effect of the finite length of the resonator on the value of its resonance frequency. Additionally, the numerical simulations provide a way to study other aspects of the performance of the resonator, e.g., the relationship between the transduction area and the insertion loss.

Different types of element models that are available in ANSYS were used to model the various components of the resonator. The mechanical beam was modeled as an orthotropic material using the SOLID95 model. The electrostatic transduction in the capacitive gaps was modeled with two arrays of TRANS126 elements generated by the EMTGEN macro after the beam had been meshed. TRANS126 is a transducer element that uses a simple capacitive model to simulate the interaction between the electrostatic and mechanical domains. It is suitable for use both in structural finite-element analysis and in electro-mechanical circuit simulation. The EMTGEN macro was used to generate automatically an array of TRANS126 elements in each of the capacitive gaps. The elements are connected between nodes on the surface of the silicon beam and a plane of nodes that represent the fixed electrodes. The equivalent capacitance of each element is also computed automatically by the macro, based on the area of the mesh surfaces associated with the nodes which the element is connected to.

A number of resistors and capacitors were also added to model the test setup used for resonator testing and characterization [10]. The equivalent schematic diagram of the complete ANSYS model used in the simulations is shown in Fig. 10. C_s and C_d model the gap capacitances, C_{ps} and C_{pd} model the parasitic pad capacitances, and R_S and R_L model the internal resistances of the test instruments.

The model was used to simulate the frequency response of resonators of varying dimensions. Each simulation consisted of a static analysis, which is needed to account for the effect of the dc polarization voltage, followed by a harmonic (i.e., a frequency domain) analysis over a certain frequency range. This particular set of analyses, combined with the inclusion of the electrostatic gap in the model, provides a more comprehensive and accurate information about the behavior of the complete device than what is obtainable from a simple modal analysis. In particular, the simulation results include the values of all of the node voltages, which makes it possible to generate plots of the voltage gain $A_v = v_{out}/v_{in}$ over the specified range of

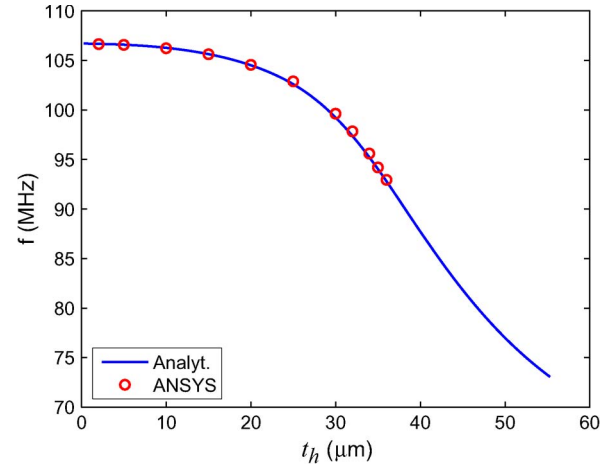


Fig. 11. Resonance frequency versus SiBAR thickness.

frequencies. Many parameters that are related to the resonator performance can then be evaluated based on the location and magnitude of the peaks in the graph of $|A_v|$, including the effects of the resonator dimensions, the polarization voltage, and the magnitude of the capacitive gaps not only on the resonance frequency but also on the insertion loss.

Before discussing the results of the simulations, the selection of one particular parameter in the ANSYS model merits an additional comment, namely, the value of the damping ratio used by ANSYS in its harmonic analysis (DMPRAT). This parameter was used to account for the total energy losses in the resonator. In the absence of a reliable model for those losses, the value of DMPRAT was chosen so that the simulated insertion loss of the resonator would approximately match the previously measured insertion losses of similar resonators in the frequency range of interest. Consequently, the ANSYS model described herein cannot be used to obtain reliable *a priori* estimates of the insertion loss of a resonator. On the other hand, the model can be expected to provide reasonably accurate information, for example, about how changes in the resonator dimensions affect the overall voltage gain A_v , provided that its resonance frequency does not deviate excessively from the value that is used to select the value of the damping ratio, in the first place. This is based on the assumption that the rate of energy losses does not change dramatically within a relatively narrow frequency range.

The model described earlier was used to simulate a set of (100, 011) SiBARs having the same length (400 μm) and width (40 μm) but with varying thicknesses. The values of the thicknesses were chosen so that the main resonance peak would fall on the first dispersion curve. Brick meshing was used, and the mesh size was chosen so that the number of elements generated would be on the order of a few tens of thousands.

Fig. 11 compares the values of the resonance frequency obtained from the ANSYS simulations, determined by the location of the main peak in the output voltage, with those predicted by the dispersion curves generated by (7). The ANSYS simulation results are reported only for those devices in which the peak that corresponds to the resonance mode of interest could be identified with some certainty. When the device thickness exceeds a certain value (approximately 35 μm for the examples shown in Fig. 11), the location of the peak (or even

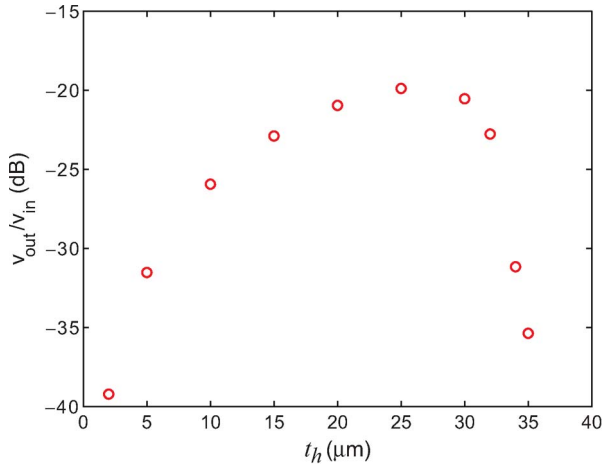


Fig. 12. Voltage gain versus SiBAR thickness on the first dispersion curve.

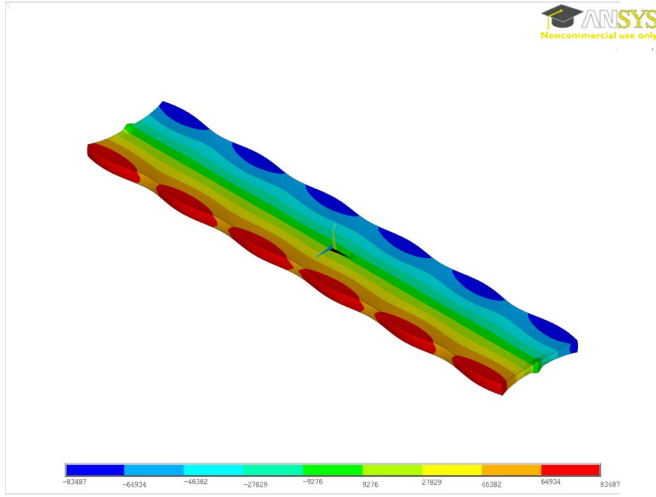


Fig. 13. Resonance mode shape of a SiBAR of dimensions 400 μm (L) by 40 μm (W) by 10 μm (t_h).

the existence of one) becomes difficult to determine because the amplitude of the peak becomes progressively smaller (see Fig. 12), and multiple peaks become visible in the vicinity of the frequency predicted by (7) (see Fig. 15). These two phenomena will be discussed in more detail later in this section. It can be seen that, as long as an identifiable peak in the frequency response can be found, the two models are in excellent agreement. The difference between the computed values of the resonance frequencies is on the order of a few hundreds of kilohertz.

As indicated previously, the amplitude of the peak in the output voltage can be used to compute the value of the overall voltage gain A_v at resonance. The plot of the simulated values of $|A_v|$ is shown in Fig. 12. As shown in the figure, at first, the magnitude of the voltage gain increases with the thickness of the device due to the corresponding increase in the capacitive gap transduction area. Beyond a certain point, however, further increases in the thickness actually cause the voltage gain to decrease. This phenomenon can be explained, at least in part, by a decrease in the efficiency of the electrostatic transduction in the capacitive gaps [13]. More specifically, for relatively small values of the thickness, the shape of the resonance mode is almost purely extensional, as shown in Fig. 13. This means that

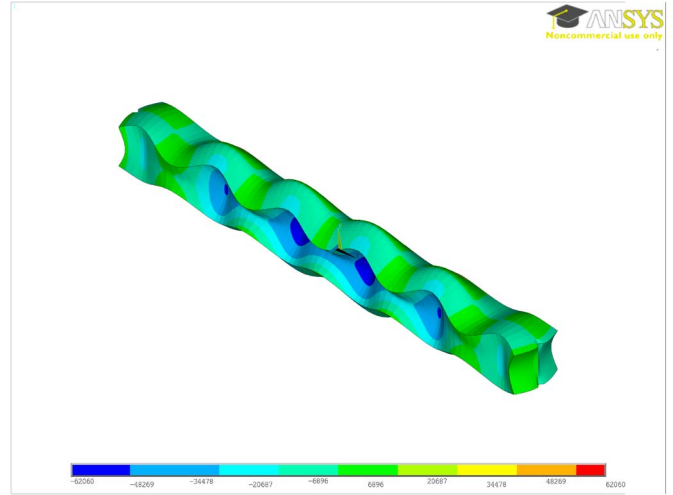


Fig. 14. Resonance mode shape of a SiBAR of dimensions 400 μm (L) by 40 μm (W) by 35 μm (t_h).

the side of the bar that faces the capacitive gap remains almost flat, causing the changes in the gap capacitance to be essentially proportional to the changes in the width of the bar.

As the bar thickness increases, the shape of the resonance mode becomes more complex, and peaks and valleys start to appear on the face of the resonator that defines the capacitive gap, as shown in Fig. 14. This evolution in the mode shape has two consequences: The first is that changes in the resonator width do not translate directly into changes in the gap capacitance, and the efficiency of the electrostatic transduction decreases. Eventually, this decrease overtakes the gain due to larger transduction areas, and the overall voltage gain starts to decrease as well, as shown in Fig. 12. The second consequence is that the assumption that the displacement in the width direction (u_z) is independent of x becomes less valid. Since this was one of the assumptions that were made at the outset of the derivation of the analytical model, a degradation in its accuracy can be expected as the thickness of the SiBAR increases. This explains why Fig. 11 shows a slight increase in the difference between the values of the resonance frequencies yielded by the analytical and numerical models for thickness values larger than 25 μm .

The ANSYS simulations of this particular resonator also show that, when its thickness exceeds values of about 30 μm , two peaks become apparent in the vicinity of the frequency given by (7) (see Fig. 15). This indicates the presence of an additional resonance mode, which does not belong to the class of modes analyzed in Section II. The appearance of multiple resonance modes close to the frequency predicted by (7) seems to be linked to a simultaneous change of sign in two subexpressions of (7), namely, $(c_{22}\alpha^2 - c_{23}u_{z0})$ and $(u_{y1} - \beta^2)$. It is possible to show that both expressions become zero when $v = v_c$, where v_c is defined by

$$\rho v_c^2 = \frac{c_{22}c_{33} - c_{23}^2}{c_{22} + c_{23}}.$$

For $v > v_c$, both expressions are negative, while for $v < v_c$, they are both positive. From (7), it is readily seen that $v = v_c$

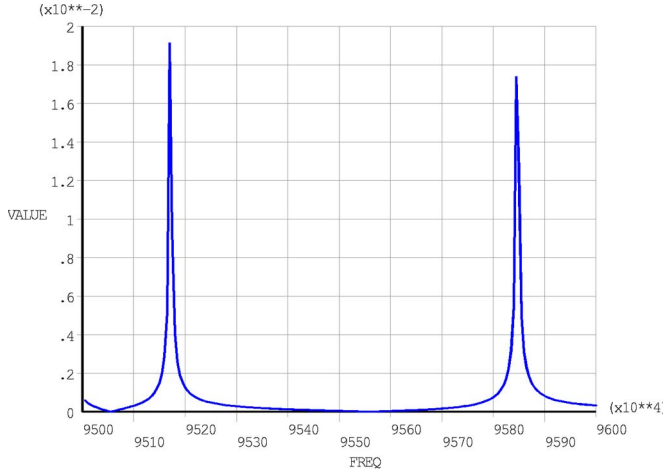


Fig. 15. Frequency response of a SiBAR of dimensions $400\ \mu\text{m}$ (L) by $40\ \mu\text{m}$ (W) by $34\ \mu\text{m}$ (t_h) obtained from the ANSYS simulations, showing two closely resonance modes.

when $\cos \pi \beta_c \xi = 0$, i.e., when $\xi = \xi_c = 1/(2\beta_c)$, where β_c is the value of β that corresponds to v_c , which is expressed as

$$\beta_c^2 = \frac{c_{23} + c_{33}}{c_{23} + c_{22}}.$$

In summary, the ANSYS simulation results confirm the existence of resonance modes on the top portion of the first dispersion curve generated by (7). They also show that those modes induce a detectable peak in the electrical frequency response of a capacitive SiBAR and that the amplitude of that peak initially increases with the thickness of the SiBAR. The peak amplitude, however, reaches a maximum and then starts to decrease as the SiBAR thickness increases further and as the value of ξ approaches ξ_c . Simultaneously, multiple peaks start to appear in the vicinity of the frequency predicted by (7). Thus, from a practical point of view, ξ_c appears to set an upper bound on the t_h/W ratio of a SiBAR. Because of the high insertion loss and the presence of multiple resonance peaks, SiBAR operation on the first dispersion curve for values of ξ exceeding or even approaching ξ_c does not seem to be practically possible, unless the efficiency of electromechanical transduction in the capacitive gaps can be somehow improved.

Note that $\beta_c = 1$ whenever $c_{22} = c_{33}$, and this equality holds in all isotropic materials and also in single-crystal silicon when propagation occurs along one of the $\langle 100 \rangle$ crystallographic axes. In such case, $\xi_c = 1/2$, and the corresponding aspect ratio is $t_h/W = 1/n_z$. In the case of the propagation along one of the $\langle 110 \rangle$ axes, $\xi_c = 0.4714$, which is equivalent to $t_h/W = 0.9428/n_z$. If $W = 40\ \mu\text{m}$, the corresponding upper bound on the SiBAR thickness is $t_h = 37.7\ \mu\text{m}$ for $n_z = 1$, which is a value that is in good agreement with the ANSYS simulations. Note that, if the same SiBAR was to be operated in the third-order mode ($n_z = 3$), then its maximum thickness would be $37.7/3 \approx 12.6\ \mu\text{m}$.

The ANSYS simulations of SiBARs operating on the second dispersion curve in Fig. 5 also showed peaks at frequencies close to those predicted by the analytical model. The amplitude of those peaks, however, was significantly smaller than that of the peaks observed on the first dispersion curve, to the point that

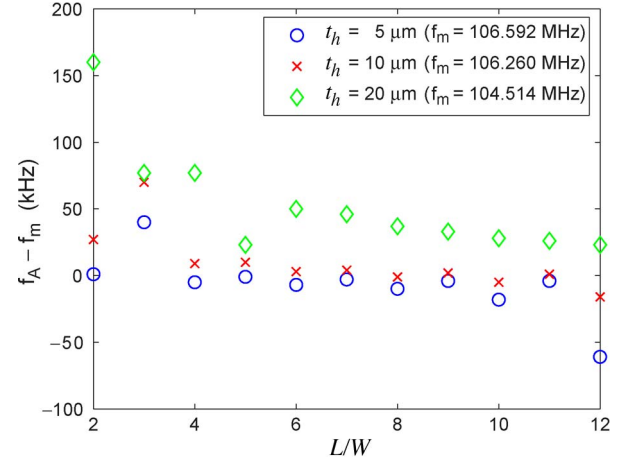


Fig. 16. Difference between the simulated and analytical resonance frequencies versus the length-to-width ratio in SiBARs of varying thicknesses ($W = 40\ \mu\text{m}$).

operation of those devices on the portion of the curve covered by the simulations would be practically unfeasible. Since the time needed for numerical simulations increases dramatically with the dimensions of the resonator, it was impossible to verify the existence or the amplitude of the resonance peaks on the dispersion curves beyond the first two.

Finally, a further set of ANSYS simulations was run to determine the effect of the length of a SiBAR on its resonance frequency. The simulated SiBARs had a width of $40\ \mu\text{m}$, length-to-width ratios ranging from 2 to 12, and thicknesses of 5, 10, and $20\ \mu\text{m}$, which span the typical thickness range of fabricated SiBARs. Fig. 16 shows $f_A - f_m$ versus L/W , where f_A is the value of the resonance frequency obtained from ANSYS modal analysis, while f_m is the resonance frequency computed by the analytical model (which assumes an infinitely long SiBAR). It can be seen that the relative difference between the two values is typically on the order of 0.1% or less, with the maximum being about 160 kHz or 0.16% for a $20\text{-}\mu\text{m}$ -thick SiBAR, with $L/W = 2$. A visual examination of the mode shapes explains why the analytical model remains so accurate: The basic mathematical assumptions underlying the model ($u_x = 0$ and u_y and u_z are independent of x) are still approximately valid even at low L/W ratios. In other words, the shape of these resonance modes is almost purely width extensional, even in the case of relatively short SiBARs.

In summary, the ANSYS model described in this section can be used to obtain additional information about the behavior of capacitive BARs, which is not available from the analytical model of Section II. Taken together, those two models provide an effective tool that can be used to design and optimize the performance of this type of resonators: For example, they make it possible to select the SiBAR thickness so as to minimize the insertion loss caused by the resonator [20].

VI. EXPERIMENTAL RESULTS

Both the analytical and numerical models, described in Sections II and V, respectively, were validated against the measurements taken on SiBARs of various dimensions, fabricated

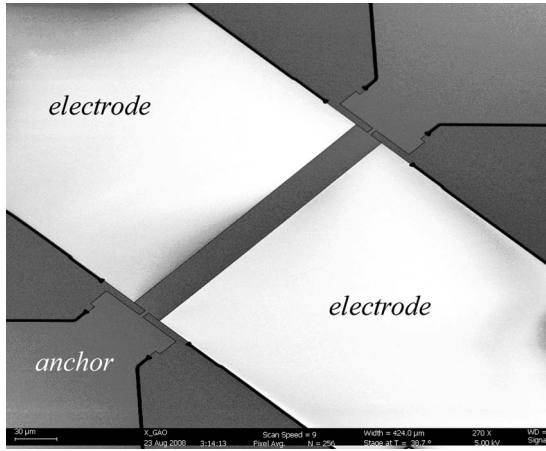


Fig. 17. SEM view of a SiBAR fabricated in a 10- μm -thick SOI with a capacitive gap of 300 nm.

using a two-mask process on low-resistivity (100) silicon-on-insulator (SOI) wafers with a device layer thickness of 10 μm . The first mask layer, which is a thin layer of thermal oxide, was defined using electron-beam lithography, using ZEP 520 as the photoresist for submicrometer-wide capacitive trench patterning. The oxide mask was then patterned in CF_4 and H_2 plasma.

The residual ZEP layer was removed in oxygen plasma before silicon etching. A deep reactive ion etching tool (STS Pegasus) was used in this step to etch and define the resonating bar. Since the Bosch process was applied in Pegasus, the sample was cleaned in a Piranha bath, followed by oxygen plasma clean to remove any polymer residue on the sidewalls of the trenches. The remaining oxide mask was removed by a short immersion in a buffered oxide etchant.

The second mask was defined with photolithography to isolate the electrodes. Shipley resist 1827 was used as the mask to define the electrodes. The width of the trench patterns around these electrodes is 3 μm . The trench etching process took place in an STS inductively coupled plasma etcher, which fits the purpose of obtaining a lower selectivity and aspect-ratio process compared to the capacitive trench etching process. Again, Piranha and oxygen plasma clean were applied to the sample to remove any polymer residue on the sample surface or inside the trenches due to polymer passivation in the Bosch process and photoresist bridging over submicrometer-width trenches. Both (100, 011) and (100, 010) SiBARs were fabricated on the same wafer. Scanning electron micrographs (SEMs) of a sample device are shown in Figs. 17 and 18.

An Agilent E5071C network analyzer was then used to measure the electrical resonance frequencies of the fabricated SiBARs. The measured resonance frequencies of various devices are reported in Table I, together with the values predicted by the analytical and numerical models and by (1). The value of W that was used in all calculations was the actual measured width of the device, so that the comparison would not be affected by process variations. The values of the stiffness coefficients used in the analytical and ANSYS models were taken from the scientific literature. Specifically, $c_{22} = c_{33} = 165.7$, $c_{23} = 63.9$, and $c_{44} = 79.6$ GPa were used for

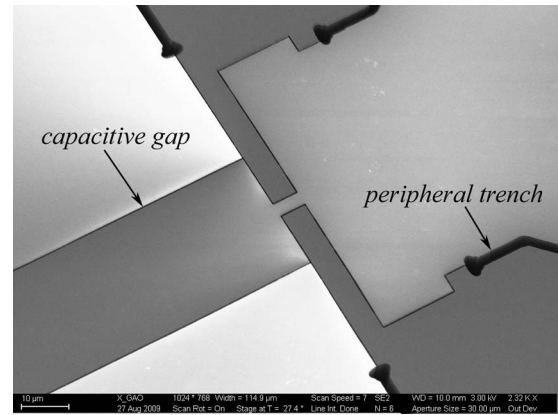


Fig. 18. Detailed SEM view of the area at one end of a SiBAR.

the (100, 010) resonators [18], while an appropriate coordinate transformation yielded $c_{22} = 165.7$, $c_{33} = 194.4$, $c_{23} = 63.9$, and $c_{44} = 79.6$ GPa for the (100, 011) resonators. In (1), E was set to the values of Young's modulus for silicon in the [011] or [010] directions of the (100) plane (i.e., 169 GPa for the (100, 011) devices and 130 GPa for the (100, 010) devices [18]).

A comparison of the data reported in Table I shows that both models can predict the resonance frequency of a SiBAR with an accuracy that, in most cases, is significantly better than 1%. The close agreement among the three sets of data validates the assumptions made in the derivation of the analytical model in Section II. In particular, it confirms that SiBARs, whose length is dominant compared to the other dimensions, support, among others, a set of resonance modes that can be analyzed with good approximation by assuming the length of the resonator to be infinite. In practice, this means that the resonance frequency of those modes is, to a large extent, independent of the length of the resonator. All practical applications of SiBARs that have appeared in the literature to date rely on this particular set of modes.

The data in Table I also confirm that (1) should be regarded as just a first-order approximation of the resonance frequency of a SiBAR. The accuracy of that approximation decreases as the ratio $\xi = t_h/\lambda_z = n_z t_h/2W$ increases. This is a result of the fact that (1) yields a value that is independent of the SiBAR thickness, while in reality, there is a gradual decrease in the resonance frequency of the device as its thickness increases, which is an effect that is correctly predicted by both the analytical and numerical models.

Finally, Fig. 19 shows the measured and simulated electrostatic tuning characteristics of a 108-MHz SiBAR with 135-nm capacitive gaps. The measured frequency values were taken from [10, Fig. 10]. The simulations were performed using the ANSYS model described in Section V, with the value of the resonance frequency being determined by the location of the peak of the frequency response computed by the model. The value of the SiBAR width in the model was chosen so that the simulated resonance frequency at $V_p = 10$ V matched as closely as possible the actual measurement and remained fixed as the value of the polarization voltage was changed. This was done to make it easier to evaluate the ability of the model to track the relationship between the resonance frequency and

TABLE I
COMPARISON BETWEEN THE PREDICTED AND MEASURED SiBAR RESONANCE FREQUENCIES

Length (μm)	Width (drawn) (μm)	Width (meas.) (μm)	SiBAR Type	Mode order (n_z)	Res. freq. (meas.) (MHz)	Analytical Freq. (MHz)	Error (%)	ANSYS model Freq. (MHz)	Error (%)	Equation (1) Freq. (MHz)	Error (%)
310	40	39.97	100,011	1	106.308	106.34	0.03	106.23	-0.07	106.5	0.18
				3	299.082	297.92	-0.40	297.85	-0.41	319.61	6.86
400	40	39.86	100,011	1	106.5	106.6	0.09	106.59	0.08	106.8	0.28
216	27	26.94	100,011	1	157.064	156.84	-0.14	156.86	-0.13	158.1	0.66
270	27	26.96	100,011	1	157.062	156.73	-0.21	156.74	-0.20	157.9	0.53
240	24	23.91	100,011	1	176.452	176.12	-0.19	176.17	-0.16	178.1	0.93
200	20	19.90	100,011	1	210.628	209.97	-0.31	210.06	-0.27	214	1.6
240	30	29.86	100,010	1	128.265	129.30	0.81	129.01	0.58	125.1	-2.47
				3	330.748	330.61	-0.04	330.97	0.07	375.2	13.44
360	45	44.51	100,010	1	85.815	87.12	1.52	86.90	1.26	83.91	-2.22
				3	248.116	250.62	1.01	250.61	1.00	251.7	1.44
360	60	59.74	100,010	1	64.586	65.01	0.66	65.06	0.73	62.52	-3.20

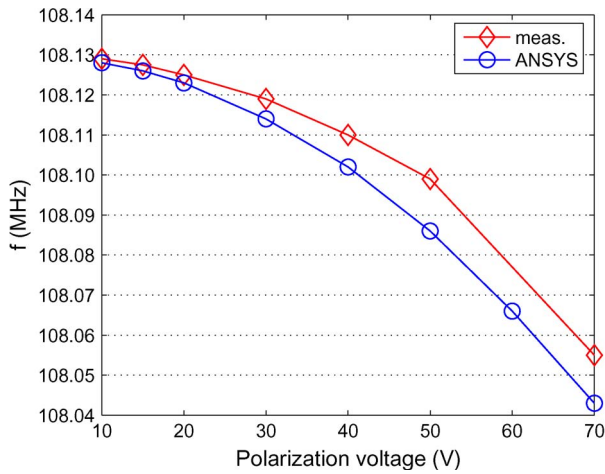


Fig. 19. Measured and simulated electrostatic tuning characteristics of a 108-MHz SiBAR.

the polarization voltage. As shown in Fig. 19, the agreement between the simulations and the measurements is very good. The slight divergence in the two graphs at the higher voltages is due to the fact that the simulations were based on the nominal value of the capacitive gap (135 nm), while a least-square fit of the measured data yields an actual gap size of approximately 151 nm.

VII. CONCLUSION

Quantitatively accurate compact device models are useful because they shed light on the behavior of the device, in addition to being valuable design aids. The analysis of SiBARs presented in this paper, although far from complete, nevertheless yields useful qualitative and quantitative information about the operation of those resonators. For example, it provides a fairly accurate characterization of the resonance modes that determine the behavior of SiBARs in practical applications. If the SiBAR is sufficiently long, the resonance frequencies of those modes are essentially independent of the length of the resonator, and they can be calculated with a very good approximation by assuming an infinitely long device. Moreover, the analysis reveals that the anisotropic characteristics of the material play a nonnegligible role in determining the wave propagation velocity and, consequently, the values of the

resonance frequencies. This means that an accurate calculation of those frequencies cannot be made by assuming the material to be isotropic.

The finite-element SiBAR model makes it possible to perform a more refined analysis and to compute performance parameters that cannot be obtained from the analytical model, such as the change in the resonance frequency of the device due to changes in the polarization voltage or the relationship between the electrostatic transduction area and the insertion loss. Taken together, these two models can be effective aids in the design of high-performance SiBARs.

The results presented in this paper also identify several areas that warrant further research. One of them is the development of an analytical model of the insertion loss associated with a particular resonance mode and, in particular, of the relationship between the insertion loss and the resonator dimensions. The analysis carried out in Section II yields a set of dispersion curves, such as those shown in Figs. 4–6, and each point on any of those curves is potentially associated with a resonance mode. While the numerical model of Section V confirms the existence of those modes, it also reveals that the insertion loss can vary dramatically between modes that lie on different curves or even on different sections of the same curve. An analytical model that is capable of predicting the insertion loss associated with a given resonance mode would not only be more useful for the purpose of designing a SiBAR that meets certain performance objectives, but it would also give some insights into the physical mechanisms that determine the insertion loss.

It is also apparent from the numerical simulations that SiBARs support resonance modes other than those analyzed in Section II. Conceivably, the resonance frequencies of those modes depend on the length of the resonator, which is a feature that is potentially useful in applications that require banks of resonators with slightly different frequencies. For this reason, it would be of both theoretical and practical interest to develop a more comprehensive SiBAR analytical model characterizing those additional modes.

Finally, the simulations seem to suggest that some of the resonance modes identified by the analytical model may be unstable and thus incapable of being supported by a physical resonator. In fact, as explained in Section V, the degradation in the insertion loss observed when the SiBAR thickness exceeds a certain threshold may be due, in part, to the fact that the mode is

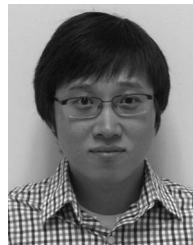
approaching the boundary of its stability region. For this reason, a theoretical analysis of the stability of the resonance modes identified by the analytical model presented in this paper or by other more comprehensive models that may be developed in the future would be useful in determining which modes can actually exist in a physical resonator and also in evaluating the insertion loss associated with a particular mode.

REFERENCES

- [1] M. A. Abdelmoneum, M. U. Demirci, and C. T.-C. Nguyen, "Stemless wine-glass-mode disk micromechanical resonators," in *Proc. 16th IEEE Int. Conf. Micro Electro Mech. Syst.*, Kyoto, Japan, Jan. 2003, pp. 698–701.
- [2] J. Wang, Z. Ren, and C. T.-C. Nguyen, "Self-aligned 1.14 GHz vibrating radial-mode disk resonators," in *Proc. Tech. Dig. 12th Int. Conf. Solid-State Sens., Actuators Microsyst. (TRANSDUCERS)*, Boston, MA, Jun. 2003, vol. 2, pp. 947–950.
- [3] S. Pourkamali and F. Ayazi, "SOI-based HF and VHF single-crystal silicon resonators with sub-100 nanometer vertical capacitive gaps," in *Tech. Dig. 12th Int. Conf. Solid-State State Sens., Actuators Microsyst. (TRANSDUCERS)*, Boston, MA, Jun. 2003, vol. 1, pp. 837–840.
- [4] Y.-W. Lin, S. Lee, S.-S. Li, Y. Xie, Z. Ren, and C. T.-C. Nguyen, "Series-resonant VHF micromechanical resonator reference oscillators," *IEEE J. Solid-State Circuits*, vol. 39, no. 12, pp. 2477–2491, Dec. 2004.
- [5] J. Wang, Z. Ren, and C. T.-C. Nguyen, "1.156 GHz self-aligned vibrating micromechanical disk resonator," *IEEE J. Solid-State Circuits*, vol. 51, no. 12, pp. 1607–1628, Dec. 2004.
- [6] S. Pourkamali and F. Ayazi, "High frequency capacitive micromechanical resonators with reduced motional resistance using the HARPSS technology," in *Proc. Top. Meeting Silicon Monolithic Integr. Circuits RF Syst.*, Atlanta, GA, Sep. 2004, pp. 147–150.
- [7] J. R. Clark, W.-T. Hsu, M. A. Abdelmoneum, and C. T.-C. Nguyen, "High- Q UHF micromechanical radial-contour mode disk resonators," *J. Microelectromech. Syst.*, vol. 14, no. 6, pp. 1298–1310, Dec. 2005.
- [8] S. Pourkamali, G. K. Ho, and F. Ayazi, "Vertical capacitive SiBARs," in *Proc. 18th IEEE Int. Conf. Micro Electro Mech. Syst.*, Miami, FL, Jan. 2005, pp. 211–214.
- [9] S. Pourkamali, G. K. Ho, and F. Ayazi, "Low-impedance VHF and UHF capacitive silicon bulk acoustic wave resonators—Part I: Concept and fabrication," *IEEE Trans. Electron Devices*, vol. 54, no. 8, pp. 2017–2023, Aug. 2007.
- [10] S. Pourkamali, G. K. Ho, and F. Ayazi, "Low-impedance VHF and UHF capacitive silicon bulk acoustic wave resonators—Part II: Measurement and characterization," *IEEE Trans. Electron Devices*, vol. 54, no. 8, pp. 2024–2030, Aug. 2007.
- [11] A. K. Samaroo, G. Casinovi, and F. Ayazi, "Passive TCF compensation in high Q silicon micromechanical resonators," in *Proc. IEEE Int. Conf. Micro Electro Mech. Syst.*, Hong Kong, Jan. 2010, pp. 116–119.
- [12] R. Tabrizian, M. Rais-Zadeh, and F. Ayazi, "Effect of phonon interactions limiting the fQ product of micromechanical resonators," in *Proc. Tech. Dig. 15th Int. Conf. Solid-State Sens., Actuators Microsyst. (TRANSDUCERS)*, Denver, CO, Jun. 2009, pp. 2131–2134.
- [13] G. K. Ho, "Design and characterization of silicon micromechanical resonators," Ph.D. dissertation, Georgia Inst. Technol., Atlanta, GA, 2008.
- [14] G. Casinovi, X. Gao, and F. Ayazi, "Analytical modeling and numerical simulation of capacitive silicon bulk acoustic resonators," in *Proc. IEEE Int. Conf. Micro Electro Mech. Syst.*, Sorrento, Italy, Jan. 2009, pp. 935–938.
- [15] R. D. Mindlin, "Waves and vibrations in isotropic, elastic plates," in *Structural Mechanics*, J. N. Goodier and N. J. Hoff, Eds. Oxford, U.K.: Pergamon, 1960, pp. 199–232.
- [16] K. F. Graff, *Wave Motion in Elastic Solids*. New York: Dover, 1991.
- [17] J. F. Rosenbaum, *Bulk Acoustic Wave Theory and Devices*. Boston, MA: Artech House, 1988.
- [18] J. J. Wortman and R. A. Evans, "Young's modulus, shear modulus, and Poisson's ratio in silicon and germanium," *J. Appl. Phys.*, vol. 36, no. 1, pp. 153–156, Jan. 1965.
- [19] C. L. Dym and I. H. Shames, *Solid Mechanics: A Variational Approach*. New York: McGraw-Hill, 1973.
- [20] H. M. Lavasani, A. K. Samaroo, G. Casinovi, and F. Ayazi, "A 145 MHz low phase-noise capacitive silicon micromechanical oscillator," in *IEDM Tech. Dig.*, San Francisco, CA, Dec. 2008, pp. 675–678.



mechanical systems.



Giorgio Casinovi (M'89–SM'93) received B.S. degrees in electrical engineering and in mathematics from the University of Rome, Rome, Italy, in 1980 and 1982, respectively, and the M.S. and Ph.D. degrees in electrical engineering from the University of California, Berkeley, in 1984 and 1988, respectively. He has been with the School of Electrical and Computer Engineering, Georgia Institute of Technology, Atlanta, since 1989. His research interests include computer-aided design and simulation of electronic devices, circuits, and microelectro-

Xin Gao received the B.S. and M.S. degrees in electrical and computer engineering from Georgia Institute of Technology, Atlanta, in 2004 and 2005, respectively, where he is currently working toward the Ph.D. degree in electrical and computer engineering.

His research focuses on the development of silicon deep reactive ion etching processes for MEMS resonators, through silicon vias, and passives.



Farrokh Ayazi (S'96–M'00–SM'05) received the B.S. degree from the University of Tehran, Tehran, Iran, in 1994, and the M.S. and Ph.D. degrees from the University of Michigan, Ann Arbor, in 1997 and 2000, respectively, all in electrical engineering.

He joined the faculty of Georgia Institute of Technology, Atlanta, in December 1999, where he is currently a Professor in the School of Electrical and Computer Engineering. He is the Cofounder and Chief Technology Officer (CTO) of Qualtré Inc., which is a spin-out from his research labora-

tory that commercializes multi-axis bulk-acoustic-wave silicon gyroscopes and multidegrees-of-freedom inertial sensors for consumer electronics and personal navigation systems. His research interests are in the areas of integrated micro- and nanoelectromechanical resonators, interface IC designs for MEMS and sensors, RF MEMS, inertial sensors, and microfabrication techniques.

Prof. Ayazi is an Editor for the JOURNAL OF MICROELECTROMECHANICAL SYSTEMS. He served on the Technical Program Committee of the IEEE International Solid State Circuits Conference for six years (2004–2009). He was the recipient of an NSF CAREER Award in 2004, the 2004 Richard M. Bass Outstanding Teacher Award (determined by the vote of the ECE senior class), and the Georgia Tech College of Engineering Cutting Edge Research Award for 2001–2002.